

TWENTYFIFTH EUROPEAN ROTORCRAFT FORUM

Paper n° G6

ACTIVE CONTROL OF VIBRATIONS DUE TO BVI  
AND EXPERIMENTAL CORRELATION

BY

M. DE TERLIZZI, P. P. FRIEDMANN  
UNIVERSITY OF MICHIGAN, USA

SEPTEMBER 14 - 16, 1999  
ROME  
ITALY

ASSOCIAZIONE INDUSTRIE PER L'AEROSPAZIO, I SISTEMI E LA DIFESA  
ASSOCIAZIONE ITALIANA DI AERONAUTICA ED ASTRONAUTICA

# ACTIVE CONTROL OF VIBRATIONS DUE TO BVI AND EXPERIMENTAL CORRELATION

M. de Terlizzi\* and P.P. Friedmann†  
 Department of Aerospace Engineering  
 University of Michigan  
 Ann Arbor, Michigan 48109-2140

## ABSTRACT

This paper describes vibratory load reduction due to blade vortex interaction (BVI) using an actively controlled trailing edge flap (ACF). Two aeroelastic models capable of simulating the vibration reduction process have been developed. The first uses quasisteady aerodynamics for the calculation of blade loads; the second employs a new compressible unsteady aerodynamic model. Both models are combined with a free wake simulation capability for capturing the effects of BVI. Reduction of 4/rev vibratory hub loads was studied in a four-bladed hingeless rotor. Results from the simulation were compared with experimental data. The vibration reduction study indicates that the ACF has remarkable potential for reducing vibratory hub loads induced by BVI. Good correlation with experimental results relative to 2/rev, 3/rev, 4/rev and 5/rev flap actuation was obtained.

## LIST OF SYMBOLS

$c_b$  Blade chord  
 $c_{cs}$  Control surface chord  
 $C_{d0}$  Blade profile drag coefficient  
 $C_f$  Flap correction factor  
 $C_W$  Weight coefficient of the helicopter  
 $\mathbf{C}$  Assembled damping matrix  
 $D_0, D_1$  Generalized flap motions  
 $\mathbf{f}_b$  Vector of blade equations  
 $\mathbf{f}_t$  Vector of trim equations  
 $EI_y, EI_z$  Blade bending stiffnesses in flap and lead-lag, respectively  
 $\mathbf{F}$  Assembled load vector  
 $J$  Controller performance index  
 $k_A$  Polar radius of gyration of blade cross section,  $k_A^2 = (EI_y + EI_z)/EA$   
 $k_m$  Mass radius of gyration of blade cross section,  $k_m^2 = k_{m1}^2 + k_{m2}^2$  - per unit length

$k_{m1}, k_{m2}$  Principal mass radii of gyration of the cross section - per unit length  
 $\mathbf{K}$  Assembled stiffness matrix  
 $l_e$  Length of beam element  
 $L_b$  Blade length  
 $L_{cs}$  Control surface length  
 $m$  Blade mass per unit length  
 $\mathbf{M}$  Assembled mass matrix  
 $n_b$  Number of blades  
 $\mathbf{q}_b$  Vector of blade dofs  
 $\mathbf{q}_t$  Vector of trim parameters  
 $R$  Rotor radius  
 $\mathbf{T}$  Matrix of control sensitivities  
 $u, v, w$  Components of displacement  
 $\mathbf{u}$  Vector of control input harmonics  
 $W_0, W_1$  Generalized airfoil motions  
 $\mathbf{W}_u, \mathbf{W}_{\Delta u}, \mathbf{W}_z$  Control weighting matrices  
 $x_{cs}$  Distance from blade root to control flap midpoint  
 $X_{FA}, X_{FC}$  Horizontal offset of fuselage aerodynamic center and fuselage center of gravity from hub  
 $\mathbf{z}$  Vector of 4/rev hub loads  
 $Z_{FA}, Z_{FC}$  Vertical offset of fuselage aerodynamic center and fuselage center of gravity from hub  
 $\alpha$  Amplitude of warping  
 $\alpha_R$  Rotor trim pitching angle  
 $\beta_p$  Blade precone angle  
 $\gamma$  Lock number  
 $\gamma_{x\zeta}, \gamma_{x\eta}, \bar{\gamma}_{x\eta}, \bar{\gamma}_{x\zeta}$  Shear strain components, overbars denote strain at elastic axis  
 $\theta_0, \theta_{1c}, \theta_{1s}$  Collective and cyclic pitch components  
 $\theta_p$  Tail rotor collective pitch  
 $\bar{\lambda}_i$  Induced velocity vector  
 $\Lambda_a, \Lambda_s$  Tip anhedral (positive up) and sweep (positive aft)  
 $\mu$  Advance ratio  
 $\phi$  Elastic twist angle of blade  
 $\phi_R$  Rotor trim rolling angle  
 $\psi$  Azimuth angle  
 $\sigma$  Rotor solidity ratio  
 $\Omega$  Rotor angular velocity

\*Postdoctoral Scholar

†François-Xavier Bagnoud Professor of Aerospace Engineering

## 1 INTRODUCTION

An important source of higher harmonic airloads on helicopter blades, at lower advance ratios, is the phenomenon known as blade-vortex interaction (BVI) [1]. It consists of a vortex-induced loading due to the interaction of a blade with the wake tip vortex generated by the preceding blades. Blade-vortex interaction is important since it has a strong effect on vibratory response at low advance ratio descent. A number of analytical and experimental studies have been focused on the BVI phenomenon [2,3], and alleviation of BVI effects has been studied using higher harmonic control [4] and individual blade control [5]. A recent study by the authors [6-8] made an important contribution towards understanding the physical mechanism of BVI, and the potential for its alleviation using the actively controlled flap. The study concluded that alleviation of BVI-induced vibratory loads is more complicated than the reduction of vibratory hub loads due to high speed forward flight. Simulation of BVI requires a refined wake analysis tool for predicting the effects of the wake vortices on the inflow distribution at the rotor disk. This aerodynamic tool must be capable of an accurate prediction of the position of the tip vortices and the overall geometry of the helicopter wake with respect to the rotor blades. Moreover, it needs to be computationally efficient, since it must be combined with the helicopter aeroelastic response solver.

The desire to develop rotorcraft having "jet smooth" ride has shifted the emphasis in the area of vibration alleviation from traditional passive means of vibration reduction such as vibration absorbers and isolators to active control strategies [9]. Among the active control approaches the actively controlled flap (ACF) based on a controlled partial span trailing edge flap located in the outboard region of the blade has emerged as a leading candidate for practical implementation. Recent analytical [10-16] and experimental [17-19] studies have confirmed the potential of the ACF to reduce vibrations in forward flight and preliminary studies have also indicated a potential application to noise reduction [20, 21]. The experimental work by Fulton and Ormiston [18, 19, 22] has provided good quality experimental data on the practical implementation of the ACF and its application to fundamental vibration reduction in the open loop mode. The tests were performed on a small scale, 7.5-ft diameter rotor in the Army/NASA 7 x 10 ft wind tunnel.

Recently, Myrtle and Friedmann [13, 14] developed a new compressible unsteady aerodynamic model for the dynamic analysis of a rotor blade/actively controlled flap combination. In vibration control studies performed using the ACF

with the new aerodynamic model [13-15], significantly higher average and instantaneous flap actuation power requirements were obtained when compared to those based on quasisteady aerodynamics. From these studies it was concluded that unsteady aerodynamics and compressibility effects need to be included in simulations of the ACF, so that more accurate specifications for flap actuation requirements is provided.

Despite the significant amount of analytical studies on the actively controlled flap, little work has been done on validating the theoretical models for the ACF versus experimental results. A comparison between analytical and experimental results is essential to validate the promising theoretical results for a real-world application. Milgram and Chopra performed a correlation study [23] between the UMARC [24] and CAMRAD/JA [25,26] analysis codes and the experimental data obtained in a wind tunnel test of the McDonnell Douglas Active Flap Rotor (AFR) conducted in the NASA-Langley 14 x 22 ft wind tunnel [21]. The results from the correlation were somewhat inconsistent, with some analytical results showing good agreement with experimental data and others exhibiting poor correlation. Ormiston and Fulton [19] presented comparisons between experimental data and results from two analytical models: a simplified rigid blade model [19] and an elastic blade representation modeled using the 2GCHAS code [27]. The primary purpose of the comparison was to interpret some dynamic phenomena observed in the experimental results therefore the variables compared were not directly related to the vibration control problem.

The overall goals of the study are: (1) the development of closed loop control strategies, in the time and frequency domain, for effective reduction of vibrations due to BVI, using an actively controlled flap, and (2) validation of the theoretical models developed versus the experimental results provided in Ref. 18. Two aeroelastic models have been developed for the purpose. The first model is employed for the aeroelastic analysis in the frequency domain using quasisteady aerodynamics to calculate the blade aerodynamic loads. The second model is used for the time domain analysis using compressible, unsteady aerodynamic theory.

The specific objectives of the paper are:

- (1) Development of an aeroelastic response simulation capability both in the time and frequency domain suitable for representing BVI effects on helicopter rotors including the new unsteady compressible aerodynamic model developed in Ref. 13.
- (2) Determine the effect of unsteady aerodynamics on BVI and its control by comparing the results

using quasisteady aerodynamics and the new unsteady model.

- (3) Conduct active control studies for BVI alleviation using the ACF in closed loop mode.
- (4) Correlate results from the aeroelastic model developed in the study with the experimental data obtained in Ref. 18.

## 2 WAKE MODEL

The aeroelastic models developed in this study are combined with a free wake analysis from which the nonuniform induced velocity distribution at the rotor disk is calculated. The rotor wake model used in the study has been extracted from the comprehensive rotor analysis code CAMRAD/JA [25, 26] distributed by Johnson Aeronautics. It consists of a wake geometry model, which determines the position of the wake vorticity in space, and a wake calculation model, which calculates the nonuniform induced velocity distribution given the wake geometry.

The wake geometry routine was developed by Scully [28]. The wake vorticity is created in the flow field as the blade rotates, and then convected with the local velocity of the fluid. The local velocity of the fluid consists of the free stream velocity, and the wake self-induced velocity. Thus, the wake geometry calculation proceeds as follows: (1) the position of the blade generating the wake element is calculated, this is the point at which the wake vorticity is created; (2) the undistorted wake geometry is computed as wake elements are convected downstream from the rotor by the free stream velocity; (3) distortion of wake due to the wake self-induced velocity is computed and added to the undistorted geometry, to obtain a free wake geometry. The position of a generic wake element is identified by its current azimuth position  $\psi$  and its age  $\phi$ . Age implies here the nondimensional time that has elapsed between the wake element's current position and the position where it was created. By carrying out this procedure, the position of a generic wake element is written as:

$$\vec{r}_w(\psi, \phi) = \vec{r}_b(\psi - \phi) + \phi \vec{v}_W + \vec{D}(\psi, \phi) \quad (1)$$

where  $\vec{r}_b(\psi - \phi)$  is the position of the blade when it generates the wake element,  $\vec{v}_W$  is the free stream velocity, and  $\vec{D}(\psi, \phi)$  is the wake distortion, obtained by integrating in time the self-induced velocity acting on the wake element. The first term is the position at which the wake was created, the second term is the convection due to the free stream velocity, and the third is the distortion due to the self-induced velocity.

The wake calculation model, developed by Johnson [29], is based on a vortex-lattice approximation for the wake. The wake is composed of two main elements: the tip vortex, which is a strong, concentrated vorticity filament generated at the tip of the blade; and the near wake, an inboard sheet of trailed vorticity, which is much weaker and more diffused than the tip vortex. The tip vortex elements are modeled by line segments with a small viscous core radius, while the inboard wake can be represented by vortex sheet elements or by line segments with a large core radius to eliminate large induced velocities. The near wake vorticity is generally retained for only a number  $K_{NW}$  of azimuth steps behind the blade.

Figure 3 shows the wake module components and the uniform inflow calculation procedure. Given the blade displacements and circulation distribution, the wake geometry is calculated. Once the wake geometry has been determined, the procedure calculates the influence coefficients, which are stored in the influence coefficient matrix. The induced velocity distribution is obtained by conveniently multiplying the influence coefficient matrix times the circulation distribution.

## 3 AEROELASTIC MODEL FOR FREQUENCY DOMAIN ANALYSIS

### 3.1 Structural Dynamic Model

The structural dynamic model adopted has been developed in an earlier study conducted at UCLA [30]. The blade is modeled as an elastic rotating beam that consists of a straight portion and a swept tip, whose orientation with respect to the straight portion is described by a sweep angle  $\Lambda_s$ , positive aft, and an anhedral angle  $\Lambda_h$ , positive up. The blade configuration is shown in Fig. 1. The blade is modeled as a one-dimensional structure composed of a series of beam-type finite elements. A single finite element is used to model the swept tip. The model has provisions for arbitrary cross-sectional shape having multiple cells, generally anisotropic material behavior, transverse shear and out-of-plane warping. The general strain displacement relations for the beam are simplified by using an ordering scheme [31] allowing one to express the strain components in terms of seven unknown variables: the displacement components  $u, v, w$ , the elastic twist  $\phi$ , the warping amplitude  $\alpha$ , and the transverse shears at the elastic axis  $\bar{\gamma}_{x\eta}, \bar{\gamma}_{x\xi}$ . Constitutive relations are introduced based on the assumptions of linear elastic and generally orthotropic material properties.

Hamilton's principle is used to formulate the blade dynamic equations. Hermite polynomials are

used to discretize the space dependence of the element generalized coordinates: cubic polynomials are used for  $v$  and  $w$ , quadratic polynomials are used for  $\phi$ ,  $u$ ,  $\alpha$ ,  $\bar{\gamma}_{x\eta}$  and  $\bar{\gamma}_{x\zeta}$ . The resulting beam element consists of two end nodes and one internal node at its mid-point, and has a total of 23 degrees of freedom, as shown in Fig. 2. Using the interpolation polynomials and carrying out the integration over the element length, the finite element equations of motion for each beam element are written. The nonlinear blade equations of motion are obtained from a finite element assembly procedure:

$$\mathbf{M}(\mathbf{q}_b) \ddot{\mathbf{q}}_b + \mathbf{C}(\mathbf{q}_b, \dot{\mathbf{q}}_b) \dot{\mathbf{q}}_b + \mathbf{K}(\mathbf{q}_b, \dot{\mathbf{q}}_b, \ddot{\mathbf{q}}_b) \mathbf{q}_b + \mathbf{F}(\mathbf{q}_b, \dot{\mathbf{q}}_b, \ddot{\mathbf{q}}_b) = \mathbf{0} \quad (2)$$

To be able to model the BVI control problem, an actively controlled trailing edge flap was incorporated in the blade aeroelastic model. The control surface is assumed to be an integral part of the blade, attached by hinges at a number of spanwise locations (Figure 1). The flap is assumed to rotate in the plane of the blade cross section. The flap deflection is considered a controlled quantity. It is also assumed that the presence of the small flap, located in the outboard region of the blade, has a negligible effect on the blade deformation. Thus, only the inertial and aerodynamic effects associated with the flap are included in the aeroelastic model, and the structural effects due to the flap are neglected. Two modules in the original aeroelastic analysis were modified to account for the presence of the flap, namely: (1) the free vibration analysis, that produces the mode shapes and frequencies, and (2) the aeroelastic response calculation. Additional details on the implementation of the flap in the structural dynamic and aeroelastic analysis can be found in Ref. 6.

### 3.2 Aerodynamic Loads

The aerodynamic loads are calculated from a modification of Theodorsen's quasisteady aerodynamic theory [10]. To account for the effect of reverse flow on the aerodynamic loads, lift and moment are set to zero within the reverse flow region, and the drag force is reversed in direction. The implementation of this aerodynamic model is based on an implicit formulation [32] where the expressions used in the derivation of the aerodynamic loads are coded in the computer program and assembled numerically during the solution process.

### 3.3 Method of Solution

A modal coordinate transformation is performed on Eq. (2) to reduce the size of the problem.

A substitution approach [30] is used for the treatment of the axial degree of freedom, so as to properly account for the centrifugal force and Coriolis damping effects. In this approach, both the axial degree of freedom and the axial equation of motion are retained in the aeroelastic calculation. Three flap, two lag, two torsion and one axial mode are employed in the modal coordinate transformation.

The coupled trim/aeroelastic analysis in the model is based on the blade equation, corresponding to Eq. (2), which are rewritten as:

$$\mathbf{f}_b(\mathbf{q}_b, \dot{\mathbf{q}}_b, \ddot{\mathbf{q}}_b, \mathbf{q}_t; \psi) = \mathbf{0} \quad (3)$$

and the trim parameter vector is given by

$$\mathbf{q}_t = \{\alpha_R, \theta_o, \theta_{1c}, \theta_{1s}, \theta_p, \phi_R\} \quad (4)$$

The trim equations, representing the force and moment equilibrium of the helicopter in steady, level flight, can be written as

$$\mathbf{f}_t(\mathbf{q}_b, \dot{\mathbf{q}}_b, \ddot{\mathbf{q}}_b, \mathbf{q}_t; \psi) = \mathbf{0} \quad (5)$$

Three force and three moment equilibrium equations are enforced.

The coupled trim/aeroelastic response solution is solved simultaneously using the harmonic balance method. The coupled trim/aeroelastic response problem is reduced to the solution of a nonlinear algebraic system for the unknown variables represented by the trim parameters  $\mathbf{q}_t$  and the blade motion harmonics.

The combination of the aeroelastic model with the wake analysis required the implementation of a circulation iteration loop within the aeroelastic response procedure. In the circulation loop, the circulation distribution over the blade span at a number of azimuth stations is calculated and the induced velocity over the rotor disk is evaluated from the circulation. Once the blade motion has been calculated for the new induced velocity distribution, the circulation is reevaluated and convergence is tested. The iteration continues until the circulation has converged. The convergence criterion is based on the mean-square of the change in the peak bound circulation from one iteration to the next:

$$\frac{1}{J} \sum_{j=1}^J (\Delta G a_j)^2 \leq (\epsilon)^2 \quad (6)$$

where  $G a_j$  is the bound circulation peak value at the azimuth station  $j$ ,  $J$  is the number of azimuth station

at which the circulation is evaluated, and  $\epsilon$  is the convergence tolerance.

The structure of the solution of the trim/aeroelastic response with the wake module is shown in Figure 4. Coupled trim/aeroelastic response calculation requires the simultaneous solution of the trim and blade equations in the same loop, so the circulation calculation has been moved inside the trim/structural response calculation loop. The wake geometry and influence coefficient calculation has been placed outside the trim/aeroelastic response iteration.

#### 4 AEROELASTIC MODEL FOR TIME DOMAIN ANALYSIS

##### 4.1 Structural Model

For the time domain analysis, a simpler structural formulation intended for the simulation of isotropic rotor blades has been included in the second model, to reduce the computational requirements required by the unsteady compressible aerodynamics.

The hingeless rotor blade is modeled as a slender beam composed of a linearly elastic, homogeneous material, cantilevered at the hub. The blade model is taken directly from Ref. 10 and describes the fully coupled flap-lag-torsional dynamics of an isotropic blade. Small strains and finite rotations (moderate deflections) are assumed, and the Bernoulli-Euler hypothesis is used. In addition, strains within the cross-section are neglected. The equations of motion for the elastic blade consist of a set of nonlinear partial differential equations of motion, formulated in the undeformed system, with the distributed loads left in general symbolic form.

The control surfaces are assumed to be an integral part of the blade, attached at a number of spanwise locations using hinges that are rigid in all directions except about the hinge axis, constraining the control surface cross-section to pure rotation in the plane of the blade cross-section. The control surface does not provide a structural contribution to the blade, and influences the behavior of the blade only through its contribution to the blade spanwise aerodynamic and inertial loading.

##### 4.2 Aerodynamic Model

Aerodynamic loads are modeled using a blade element formulation, with sectional loads provided by a new two-dimensional unsteady compressible aerodynamic model [14] developed by Myrtle and Friedmann [13] for an airfoil/flap combination that includes unsteady freestream effects.

The aerodynamic model was developed using a rational function approximation (RFA) [33–35] approach based on the least squares, or Roger's approximation [33]. In this approach, oscillatory aerodynamic response data is used to generate approximate transfer functions that relate generalized motions to aerodynamic loads in the frequency domain.

Consider an aerodynamic system which is represented in the Laplace domain by the expression

$$\mathbf{G}(\bar{s}) = \mathbf{Q}(\bar{s})\mathbf{H}(\bar{s}), \quad (7)$$

where  $\mathbf{G}(\bar{s})$  and  $\mathbf{H}(\bar{s})$  represent Laplace transforms of the generalized aerodynamic load and generalized motion vectors, respectively. Using the Least Squares approach,  $\mathbf{Q}(\bar{s})$  can be approximated using a rational expression of the form

$$\tilde{\mathbf{Q}}(\bar{s}) = \mathbf{C}_0 + \mathbf{C}_1\bar{s} + \sum_{n=1}^{n_L} \frac{\bar{s}}{\bar{s} + \gamma_n} \mathbf{C}_{n+1}. \quad (8)$$

By using rational expressions, the approximations can be easily transformed to the time domain to yield a state space model for the aerodynamic loads that is compatible with the structural equations of motion and commonly applied control approaches.

In the present research, a two-dimensional doublet lattice method [36] based on the Possio integral equation [37] is used to generate the necessary compressible flow oscillatory response quantities for a set of generalized airfoil and flap motions over range of reduced frequencies. In addition, the values of the poles  $\gamma_n$  have been optimized to produce a minimum error approximation.

A set of generalized airfoil and flap motions designated  $W_0$ ,  $W_1$ ,  $D_0$ , and  $D_1$  were chosen which correspond to the normal velocity distributions shown in Figure 5. After defining the generalized motion vector  $\mathbf{h}(t)$  and generalized force vector  $\mathbf{f}(t)$  as

$$\mathbf{h}(t) = \begin{bmatrix} W_0(t) \\ W_1(t) \\ D_0(t) \\ D_1(t) \end{bmatrix}, \quad \mathbf{f}(t) = \begin{bmatrix} C_l(t) \\ C_m(t) \\ C_h(t) \end{bmatrix}, \quad (9)$$

the aerodynamic system in Eq.(7) can be approximated and transformed to the time domain to produce a state space aerodynamic model given by the expressions

$$\begin{aligned} \dot{\mathbf{x}}(t) &= \frac{U(t)}{b} \mathbf{R}\mathbf{x}(t) + \mathbf{E}\dot{\mathbf{h}}(t), \\ \mathbf{f}(t) &= \frac{1}{U(t)} \left( \mathbf{C}_0\mathbf{h}(t) + \mathbf{C}_1 \frac{b}{U(t)} \dot{\mathbf{h}}(t) + \mathbf{D}\mathbf{x}(t) \right). \end{aligned} \quad (10)$$

where  $\mathbf{R}$ ,  $\mathbf{E}$  and  $\mathbf{D}$  are time invariant matrices obtained by the algebraic manipulation of Eq. (8). The

aerodynamic loads  $f(t)$  are given by Eq. (11), and are a function of a set of aerodynamic states  $x(t)$ . These states are governed by the set of first order differential equations given in Eq. (10), and are driven by the generalized airfoil and flap motions contained in the vector  $h(t)$ . Additional details on the derivation of the aerodynamic model can be found in Ref. 13.

In an aeroelastic simulation, the aerodynamic state equations become coupled with the structural equations of motion and must be solved simultaneously. To account for the effect of reverse flow on the aerodynamic loads, lift and moment are set to zero within the reverse flow region, and the drag force is reversed in direction.

#### 4.3 Method of Solution

The solution of the rotary-wing aeroelastic response problem is carried out in two steps. First, spatial discretization based on Galerkin's method [38] is used to eliminate the spatial dependence, and subsequently the combined structural and aerodynamic state equations are solved in the time domain.

In this study, Galerkin's method is based on three flap, two lead-lag, and two torsional free vibration modes of a rotating beam. The free vibration modes were calculated using the first nine exact non-rotating modes of a uniform cantilevered beam.

The complete aeroelastic model for the blade and actively controlled flap consists of three sets of equations. The first two sets consist of nonlinear differential equations that describe the structural degrees of freedom and aerodynamic states. The equations of motion for the elastic blade are represented by the expression given in Eq. (3). The complete set of aerodynamic state equations are given by Eq. (10) and can be expressed as:

$$f_a(q_b, \dot{q}_b, \ddot{q}_b, x_a, \dot{x}_a, q_t; \psi) = 0. \quad (12)$$

A third set of equations represent the trim equations, representing the force and moment equilibrium in steady, level flight, which can be symbolically represented by the expression given in Eq. (5). To obtain the coupled trim/response solution, only the steady state response of the system is considered. In this case, the trim condition can be represented by the implicit nonlinear equations

$$f_t(q_t) = 0. \quad (13)$$

Evaluation of Eqs. (13) requires the steady state hub loads that correspond to the trim parameters  $q_t$ . These are obtained by integrating Eqs. (3) and (12) numerically over time, until the response solution has converged to the steady state. The trim solution  $q_t$

is obtained using a simple autopilot type controller described in Ref. 14.

The circulation loop and the wake geometry calculation are performed at each rotor revolution until overall convergence is achieved.

## 5 CONTROL APPROACH

Reduction of the 4/rev hub loads is investigated using a control approach similar to that described in Ref. 10. In this approach, a linear optimal controller is obtained based on the minimization of a performance index  $J$  which is a quadratic function of vibration magnitudes  $z$  and control input amplitudes  $u$ . At the  $i$ -th control step,

$$J = z_i^T W_z z_i + u_i^T W_u u_i + \Delta u_i^T W_{\Delta u} \Delta u_i, \quad (14)$$

where  $\Delta u_i = u_i - u_{i-1}$ .

In this study, it is assumed that the control input and resulting vibration levels are known without error. Furthermore, a linear, quasistatic, frequency domain representation of the vibratory response to control is used [9, 10], given by

$$z_i = z_{i-1} + T_{i-1}(u_i - u_{i-1}), \quad (15)$$

where  $T_{i-1}$  is a transfer matrix relating vibratory loads to changes in the control input, taken about the current control  $u_{i-1}$ :

$$T_{i-1} = \left. \frac{\partial z}{\partial u} \right|_{u_{i-1}}. \quad (16)$$

Substituting (15) into (14), and applying the condition

$$\frac{\partial J}{\partial u_i} = 0, \quad (17)$$

yields the optimal local controller, given by

$$u_i^* = -D_{i-1}^{-1} \{ T_{i-1}^T W_z z_{i-1} - W_{\Delta u} u_{i-1} - T_{i-1}^T W_z T_{i-1} u_{i-1} \}, \quad (18)$$

where

$$D_{i-1} = T_{i-1}^T W_z T_{i-1} + W_u + W_{\Delta u}. \quad (19)$$

## 6 RESULTS AND DISCUSSION

The results presented in this section are divided in two parts: (1) closed loop vibration reduction results, and (2) results illustrating correlation with experimental data.

## 6.1 Vibration Control Studies

The variables plotted are expressed in nondimensional form, using the rotor angular velocity  $\Omega$ , the blade mass per unit span  $m$  and the rotor radius  $R$  as dimensional parameters, which are combined in a suitable manner so as to nondimensionalize the pertinent quantities. The results from both aeroelastic models are obtained for a straight hingeless blade having the parameters given in Table 1.

Using the unsteady, compressible aerodynamic theory and the control law described, simultaneous reduction of 4/rev vibratory hub loads with the free wake model was examined. The results were compared with similar results obtained using quasisteady aerodynamics. Two advance ratios,  $\mu = 0.15$  and  $\mu = 0.30$ , were considered. These two cases correspond to fundamentally different vibration phenomena. At  $\mu = 0.15$  the effects of BVI are strong and represent the primary source of higher harmonic airloads, while at  $\mu = 0.30$  BVI is less significant and vibratory loads are mainly due to the high speed forward flight. Figures 6 and 7 show the baseline and controlled vibratory hub shears and moments when using the unsteady, compressible aerodynamics, which is referred to as RFA aerodynamics, and the quasisteady aerodynamics, respectively, at  $\mu = 0.15$ . Figures 8 and 9 illustrate similar results at the higher advance ratio of  $\mu = 0.30$ . The baseline vibratory loads predicted by the two models differ as much as 50%. For the vibratory vertical shear FHZ, which is the largest vibratory component, the RFA aerodynamic model predicts a value approximately 50% higher than that obtained with quasisteady aerodynamics. For both cases, however, the local controller appears to be effective at reducing the vibratory loads at both advance ratios, but its performance at the low advance ratio,  $\mu = 0.15$ , is not as good as at  $\mu = 0.30$ . This is to be expected, since at  $\mu = 0.30$  the effects of nonuniform inflow are mild, and earlier results [10] indicated that the actively control flap performed very well when uniform inflow distribution is assumed. Figures 10 and 11 illustrate the flap input for the two advance ratios obtained with RFA aerodynamics and quasisteady aerodynamics, respectively. The figures emphasize the differences between the flap input required for vibration reduction at these two advance ratios, indicating that the vibratory loads for the two cases are very different. It should be also noted that for  $\mu = 0.15$  larger flap deflections are needed for vibration alleviation. Results with RFA aerodynamics show that flap input angles as large as 15 degrees are required. For such large flap deflections nonlinear aerodynamic effects will be significant, and will be incorporated in future simulations. Therefore, these results suggest that one flap might not be sufficient for

controlling BVI induced vibrations, and a dual flap arrangement studied by Myrtle and Friedmann [15] could represent a better approach.

In figures 12 through 13 the baseline and controlled nondimensional rotating vertical shear at the root of the blade for the two advance ratios is compared. The oscillatory amplitudes of the loads in the rotating reference frame increase at  $\mu = 0.15$  when compared to  $\mu = 0.30$ , indicating that the controller alleviates BVI effects at the expense of increased blade loading. A similar increase can also be observed for the root bending moment [6].

Finally, control power requirements during vibration alleviation for RFA aerodynamics are compared with those required when using quasisteady aerodynamics in Figs. 14 and 15. The instantaneous control power is calculated from:

$$P_{cs}(\psi) = -M_{\delta}(\psi) \dot{\delta}(\psi) \quad (20)$$

where  $M_{\delta}$  is the control surface hinge moment and  $\dot{\delta}$  is the angular velocity of the control surface about its hinge. In these figures the results denoted by QS Aero - indicate quasisteady Theodorsen type aerodynamics and RFA Aero - indicate the new unsteady aerodynamic model. In Fig. 14 power requirements at the advance ratio  $\mu = 0.30$  with RFA and quasisteady aerodynamics and the free wake model are compared with the results from the uniform inflow assumption. It is evident that power requirements are larger for the free wake case. Figure 15 compares power requirements at  $\mu = 0.15$  from RFA and quasisteady aerodynamics with the free wake model. The power requirements at  $\mu = 0.15$  are approximately one order of magnitude larger than the ones relative to advance ratio  $\mu = 0.30$ . This is due to the large amplitude of the flap control angles required for BVI-induced vibration reduction. The power requirement distribution at  $\mu = 0.15$  exhibits several sharp peaks due to the higher harmonic content of the BVI-induced aerodynamic loads. Figure 15 indicates that higher average flap actuation power requirements are obtained using RFA aerodynamics.

## 6.2 Correlation with Experimental Data

The objective in this section is to validate the analytical simulation developed by comparing the results obtained from the simulation with the experimental data from Figs 8c - 8f of Ref. 18. In these plots, phase sweeps of elevon motion were performed to investigate the effect of the phase of flap motion on vibratory loads and to determine flap effectiveness at discrete elevon harmonics. The results from the phase sweeps were used in Ref. 18 to reduce root

out-of-plane bending moments based on a simple superposition model, and therefore they represent the most significant data on flap effectiveness for vibration reduction purposes provided in Ref. 18.

The flap motion employed in the phase sweep study can be analytically described as:

$$\delta(\psi) = \delta_{fi} \cos(i\psi + \phi) \quad (21)$$

where  $\phi$  is the flap motion phase and 2/rev, 3/rev, 4/rev and 5/rev harmonic motions were chosen for the flap actuation. The data points in the plots were obtained in the following manner. First, harmonic motion for the flap was chosen ( $i = 2, 5$ ), then a phase sweep was performed, acquiring data points for a series of phase angles  $\phi$ . Finally, the amplitude of the blade root flap bending moment at the frequency of the flap motion was calculated and plotted. The elevon angles in Ref. 18 are induced by a piezoelectric bimorph in which the voltage is controlled. The results in Ref. 18 indicate that the flap deflection amplitudes  $\delta_{fi}$  in the phase sweeps varied between  $4^\circ - 6^\circ$ , depending on the specific harmonic being considered. Therefore, in the simulations the value of  $\delta_{fi}$  was selected to be  $\delta_{fi} = 5^\circ$  for all the phase sweep angles.

The results were obtained on a two-bladed rotor at the rotor speed of 760 RPM and an advance ratio of  $\mu = 0.20$ . The rotor main characteristics are presented in Table 2. The two rotor blades presented some slight differences in their construction, therefore two sets of data are presented in each plot, one relative to the first blade, referred to as Blade1, the other relative to the other one, named Blade2. In addition to the phase sweep results, the baseline (denoted in the plot as uncontrolled) values of root moment amplitudes are indicated in the plots by straight lines. It is worthwhile mentioning that some additional curves presented in Fig. 8c - 8f of Ref. 18, which were obtained by a curve fitting procedure, have not been reproduced here, since they have no bearing on the correlation objective of this paper. Two sets of results have been obtained in the course of the simulations performed. The first set has been obtained using quasisteady aerodynamics. The second set is based on the unsteady, compressible aerodynamic model, which will be referred to as the RFA model. The finite element-based structural representation described in Section 3.1 has been employed in the simulations, since it can reproduce more accurately the nonuniform spanwise structural and inertial properties of the blades used in the experiment.

The results using quasisteady aerodynamics are shown in Figures 16 through 19. The results from the simulation are compared with the experimental data points from Figs. 8c - 8f, taken from

Ref. 18. Both the results for Blade1 and Blade2 are shown. Note that the blade structural and inertial parameters which have been used in the simulation represent a trade-off between Blade1 and Blade2 properties. Therefore, the results from the simulation are expected to fall somewhere between these two datasets. The baseline values of root moment harmonics have been predicted fairly well, with a maximum error of about 30% for the 3/rev root moment amplitude. Results from phase sweeps also show good overall agreement with experimental data. As expected, the results from the simulation show trends that are a trade-off between the results from Blade1 and Blade2. The larger discrepancies occur for the 2/rev moment amplitudes in Figure 16, where some data points show a difference as large as 50% from the experimental data. Furthermore, it is noteworthy that in this case a  $90^\circ$  shift seems to be present between simulation and experimental data. Results for the 3/rev, 4/rev and 5/rev harmonics, shown in Figs. (17) - (19) indicate very good agreement. It is important to mention that simulations have been computed using a flap correction factor  $C_f = 0.2$ . This is a much lower value than  $C_f = 0.6$  adopted in the control studies described in the previous section, as mentioned in Table 1. The implication of the low value of  $C_f$  is that the flap effectiveness has been overestimated in the control studies performed using quasisteady aerodynamics. Figure 20 shows the effect of the flap correction factor  $C_f$  on the 3/rev phase sweep results. In this plot, results for values of  $C_f = 0.2$ ,  $C_f = 0.4$  and  $C_f = 0.6$  are compared with experimental data. With an increase in  $C_f$ , all the values in the distribution are increased by a constant term, and the value  $C_f = 0.2$  provides the best fit with experimental data.

Results based on RFA aerodynamics are presented in Figs. 21 through 24. Similar to the quasisteady aerodynamics case, the baseline values of root moment harmonics have been predicted fairly well, with a maximum error of about 50% for the 5/rev root moment amplitude. Results from phase sweeps also show good agreement with experimental data except for the 5/rev case, where a discrepancy of 70% is evident when compared to the experimental results. The analytical results for the RFA aerodynamics have been obtained for the same value of the flap correction factor  $C_f = 0.6$  as the one used in the control studies. Therefore the control studies performed with RFA aerodynamics represent a more realistic set of data than the one obtained from quasisteady aerodynamics, where the effectiveness of the flap has been overestimated. This also explains the higher flap displacement and flap actuation power requirements for the RFA control studies when compared to those ob-

tained from quasisteady aerodynamics. It is interesting to note that the flap correction factor  $C_f$  has a completely different physical meaning for the RFA model than it has for the case of quasisteady aerodynamics. In the RFA aerodynamic model  $C_f$  is a multiplicative factor that attenuates the amplitudes of the flap generalized motions, whereas in the quasisteady aerodynamics case it reduces the aerodynamic loads due to the flap. The effect of the flap correction factor  $C_f$  in the RFA model is shown in Fig. 25 for the 3/rev phase sweep results. In this plot, results for  $C_f = 0.6$  and  $C_f = 0.4$  are compared with experiment. Increasing the value of  $C_f$  results in an increase in the magnitude of the peaks and valleys of the distribution, leaving the average value unchanged.

## 7 CONCLUDING REMARKS

Two aeroelastic response models based on two different aerodynamic theories have been developed for the simulation of BVI on helicopter rotors with partial span trailing edge flaps. The models have been compared with experimental data. The results represent an important contribution towards understanding the mechanism of BVI and its alleviation by active control. The principal conclusions are summarized below:

- (1) The mechanism of vibration reduction using the ACF is fundamentally different for BVI ( $\mu = 0.15$ ) and vibrations due to high speed forward flight ( $\mu = 0.30$ ).
- (2) When using quasisteady or RFA aerodynamics, a reduction of approximately 80% was observed for BVI vibration, while at high forward flight vibration reduction in excess of 90% is obtained. The magnitude of control angles and the harmonic content are also substantially different between these two cases.
- (3) Results from RFA aerodynamics indicate that flap input angles as large as 15 degrees may be required. For such deflections, one flap might be inadequate and a dual flap arrangement may be required.
- (4) Alleviation of BVI due to ACF increases the oscillatory root bending moments and shears in the rotating system.
- (5) Power requirements for vibration reduction in the presence of BVI are an order of magnitude higher than those needed for high speed forward flight, due to the larger magnitude of flap control angles for the  $\mu = 0.15$  case.
- (6) Higher average flap actuation power requirements for vibration reduction in the presence of BVI are obtained using RFA aerodynamics, when compared to quasisteady aerodynamics.
- (7) Simulations of phase sweeps relative to 2/rev, 3/rev, 4/rev and 5/rev flap motion were performed

and compared with experimental results from Ref. 18. Comparison between analytical and experimental data showed good correlation for most cases.

(8) Correlation study indicates that control studies performed using quasisteady aerodynamics have over-predicted the influence of the control flap, due to an excessive value of the flap correction coefficient  $C_f$ . By contrast, results from RFA aerodynamics provide more realistic information, since a more appropriate value of  $C_f$  was selected. The effect of the flap correction coefficient on the two aerodynamic models has been studied and clarified.

(9) The ACF displays exceptional potential for alleviating vibratory loads due to BVI, however this problem is more complex than vibration due to high speed flight. Refined control strategies for BVI alleviation need to be developed by incorporating information about the distance between blade tip and vortex in the objective function.

## ACKNOWLEDGEMENTS

This research was supported by Army Grant DAAH04-95-1-0005 funded by the Army Research Office with Dr. John Prater as grant monitor. The authors wish to express their gratitude to Dr. Mark Fulton for his valuable assistance in providing data for the correlation studies.

## References

- [1] Johnson, W., Airloads, Wakes and Aeroelasticity, NASA CR 177551, 1990.
- [2] Yu, Y. H., Rotor Blade-Vortex Interaction Noise: Generating Mechanisms and Its Control Concepts, AHS Specialist Meeting on Aeromechanics Technology and Product Design for the 21st Century, Bridgeport, CT, October 1995.
- [3] Yu, Y. H., Tung, C., et al., Aerodynamics and Acoustics of Rotor Blade-Vortex Interactions, *Journal of Aircraft*, Vol. 32, No. 5, 1995, pp. 970 - 977.
- [4] Kube, R. et al., HHC Aeroacoustic Rotor Tests in the German Dutch Wind Tunnel: Improving Physical Understanding and Prediction Codes, Proc. 52nd American Helicopter Society Annual Forum, Washington, DC, June 1996.
- [5] Splettstoesser, W. R. et al., The effect of Individual Blade Pitch Control on BVI Noise - Comparison of Flight Test and Simulation Result, Proc. of the 24th European Rotorcraft Forum, Marseilles, France, September 1998, pp. AC07.1 - AC07.15.

- [6] de Terlizzi, M. and Friedmann, P. P., Aeroelastic Response of Swept Tip Rotors Including the Effects of BVI, Proc. of the 54th Annual Forum of the American Helicopter Society, Washington, DC, May 1998, pp. 644 – 663.
- [7] de Terlizzi, M. and Friedmann, P. P., BVI Alleviation Using Active Control, Proc. of the 40th AIAA/ASME/ASCE/AHS/ASC Structures, Structural Dynamics and Materials Conf., AIAA Paper 99-1220, St. Louis, MO, April 1999.
- [8] de Terlizzi, M., Blade Vortex Interaction and Its Alleviation Using Passive and Active Control Approaches, Ph.D. Dissertation, University of California at Los Angeles, 1999.
- [9] Friedmann, P. P. and Millott, T. A., Vibration Reduction in Rotorcraft Using Active Control: A Comparison of Various Approaches, *Journal of Guidance, Control and Dynamics*, Vol. 18, No. 4, 1995, pp. 664 – 673.
- [10] Millott, T. A., and Friedmann, P. P., Vibration Reduction in Helicopter Rotors Using an Actively Controlled Partial Span Trailing Edge Flap Located on the Blade, NASA CR 4611, 1994.
- [11] Milgram, J. H., A comprehensive Aeroelastic Analysis of Helicopter Main Rotors with Trailing Edge Flaps for Vibration Reduction, Ph.D. Dissertation, University of Maryland at College Park, 1997.
- [12] Milgram, J. and Chopra, I., A Parametric Design Study for Actively Controlled Edge Flaps, *Journal of the American Helicopter Society*, Vol. 43, No. 2, 1998, pp. 110 – 119.
- [13] Myrtle, T. F. and Friedmann, P. P., Unsteady Compressible Aerodynamics of a Flapped Airfoil with Application to Helicopter Vibration Reduction, Proc. 38th AIAA/ASME/ASCE/AHS/ASC Structures, Structural Dynamics and Materials Conf., AIAA Paper 97-1083, Kissimmee, FL, April 1997, pp. 224 – 240.
- [14] Myrtle, T. F. and Friedmann, P. P., New Comprehensive Time Domain Unsteady Aerodynamics for Flapped Airfoils and Its Application to Rotor Vibration Reduction Using Active Control, Proc. 35th AHS Forum, Virginia Beach, VA, April 29 – May 1 1997, pp. 1215 – 1231.
- [15] Myrtle, T. F. and Friedmann, P. P., Vibration Reduction in Rotorcraft Using the Actively Controlled Trailing Edge Flap and Issues Related to Practical Implementation, Proc. of the 54th Annual Forum of the American Helicopter Society, Washington, DC, May 1998, pp. 602 – 619.
- [16] Friedmann, P. P., Myrtle, T. F., and de Terlizzi, M., New Developments in Vibration Reduction with Actively Controlled Trailing Edge Flaps, Proc. of the 24th European Rotorcraft Forum, Marseilles, France, September 1998, pp. DY07.1 – DY07.21.
- [17] Straub, F. K., Active Flap Control for Vibration Reduction and Performance Improvement, Proc. of the 51st Annual Forum of the American Helicopter Society, Fort Worth, TX, May 1995, pp. 381 – 392.
- [18] Fulton, M. V. and Ormiston, R., Small-Scale Rotor Experiments with On-Blade Elevons to Reduce Blade Vibratory Loads in Forward Flight, Proc. of the 54th Annual Forum of the American Helicopter Society, Washington, DC, May 1998, pp. 433 – 451.
- [19] Ormiston, R. and Fulton, M. V., Aeroelastic and Dynamic Rotor Response with On-blade Elevon Control, Proc. of the 24th European Rotorcraft Forum, Marseilles, France, September 1998, pp. DY10.1 – DY10.22.
- [20] Hassan, A. A., Charles, B. D., Tadghighi, H., and Sankar, L. N., Blade-Mounted Trailing Edge Flap Control for BVI Noise Reduction, NASA CR 4426, 1992.
- [21] Dawson, S. et al., Wind Tunnel Test of an Active Flap Rotor: BVI Noise and Vibration Reduction, Proc. of the 51st Annual Forum of the American Helicopter Society, Fort Worth, TX, May 1995, pp. 631 – 648.
- [22] Fulton, M. V. and Ormiston, R., Hover Testing of a Small-Scale Rotor with On-Blade Elevons, Proc. of the 53rd Annual Forum of the American Helicopter Society, Virginia Beach, VA, April 29 – May 1 1997, pp. 249 – 273.
- [23] Milgram, J., Chopra, I., and Straub, F., Rotors with Trailing Edge Flaps: Analysis and Comparison with Experimental Data, *Journal of the American Helicopter Society*, Vol. 43, No. 4, 1998, pp. 319 – 332.
- [24] Bir, G., Chopra, I., et al., University of Maryland Advanced Rotor Code (UMARC) Theory Manual, Technical report UM-AERO 94-18, July 1994.

- [25] Johnson, W., A Comprehensive Analytical Model of Rotorcraft Aerodynamics and Dynamics, Vol. I: Theory Manual, Johnson Aeronautics, Palo Alto, CA, 1988.
- [26] Johnson, W., A Comprehensive Analytical Model of Rotorcraft Aerodynamics and Dynamics, Vol. II: User's Manual, Johnson Aeronautics, Palo Alto, CA, 1988.
- [27] Rutkowski, M. J., Ruzicka, G. C., Ormiston, R. A., Saberi, H., and Jung, Y., Comprehensive Aeromechanics Analysis of Complex Rotorcraft Using 2GCHAS, *Journal of the American Helicopter Society*, Vol. 40, No. 4, 1995.
- [28] Scully, M. P., Computation of Helicopter Rotor Wake Geometry and Its Influence on Rotor Harmonic Airloads, Ph.D. Dissertation, Aeroelastic and Structures Research Laboratory, Massachusetts Institute of Technology, 1975.
- [29] Johnson, W., Wake Model for Helicopter Rotors in High Speed Flight, NASA CR 177507, 1988.
- [30] Yuan, K. A., and Friedmann, P. P., Aeroelasticity and Structural Optimization of Composite Helicopter Rotor Blades With Swept Tips, NASA CR 4665, 1995.
- [31] Friedmann, P. P., Helicopter Rotor Dynamics and Aeroelasticity: Some Key Ideas and Insights, *Vertica*, Vol. 14, No. 1, 1990, pp. 101 - 121.
- [32] Celi, R. and Friedmann, P. P., Rotor Blade Aeroelasticity in Forward Flight with an Implicit Aerodynamic Formulation, *AIAA Journal*, Vol. 26, No. 12, 1988.
- [33] Roger, K. L., Airplane Math Modeling Methods for Active Control Design, Structural Aspects of Active Controls, AGARD-CP-228, August 1977.
- [34] Edwards, J. H., Ashley, H., and Breakwell, J., Unsteady Aerodynamic Modeling for Arbitrary Motion, *AIAA Journal*, Vol. 17, No. 4, 1979, pp. 365 - 374.
- [35] Vepa, A., Finite State Modeling of Aeroelastic Systems, NASA CR-2779, 1977.
- [36] Albano, E. and Rodden, W. P., A Doublet-Lattice Method for Calculating Lift Distributions on Oscillating Surfaces in Subsonic Flows, *AIAA Journal*, Vol. 7, No. 2, February 1969, pp. 279 - 285.
- [37] Possio, C., L'Azione Aerodinamica sul Profilo Oscillante in un Fluido Compressibile a Velocita Iposonora, *L' Aerotecnica*, April 1938, (Also available as British Ministry of Aircraft Production R.T.P. translation 987).
- [38] Friedmann, P. P., Formulation and Solution of Rotary-Wing Aeroelastic Stability and Response Problems, *Vertica*, Vol. 7, No. 2, 1983, pp. 101 - 141.

Table 1: Configuration for the Vibration Reduction Studies (Servo Flap)

<u>Rotor Data</u>	
$EI_y/m\Omega^2 R^4 = 0.0106$	
$EI_z/m\Omega^2 R^4 = 0.0301$	
$GJ/m\Omega^2 R^4 = 0.001473$	
$L_b = 1.0$	$n_b = 4$
$(k_A/k_m)^2 = 2.0415$	$a = 2\pi$
$k_{m1}/R = 0.0$	$k_{m2}/R = 0.02$
$\gamma = 5.5$	$\beta_p = 0.0$
$\sigma = 0.07$	$c_b/R = 0.055$
<u>Helicopter Data</u>	
$C_W = 0.00515$	$C_{d0} = 0.01$
$Z_{FC}/R = 0.50$	$Z_{FA}/R = 0.25$
$X_{FC}/R = 0.0$	$X_{FA}/R = 0.0$
<u>Flap Data</u>	
$L_{cs} = 0.12L_b$	$c_{cs} = c_b/4$
$x_{cs} = 0.75L_b$	$C_f = 0.6$

Table 2: Configuration for the Correlation Studies (Plain Flap)

<u>Rotor Data</u>	
$N_b = 2$	$L_b = 1.0$
$\omega_{F1} = 1.11$	$e = 0.106R$
$\omega_{L1} = 1.08$	$c_b = 0.0756$
$\omega_{T1} = 4.6$	$\sigma = 0.048$
$\gamma = 6.95$	
<u>Flap Data</u>	
$x_{cs} = 0.75R$	
$L_{cs} = 0.12R$	$c_{cs} = c_b/10$

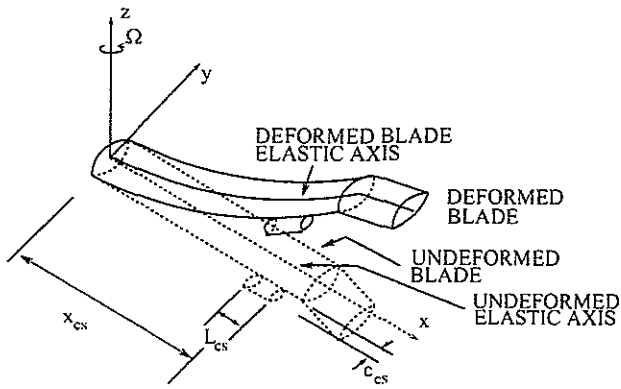


Figure 1: Schematic model of hingeless blade with actively controlled partial span trailing edge flap.

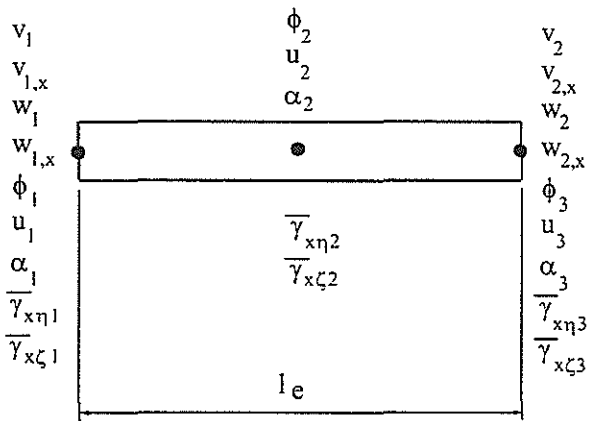


Figure 2: Finite element degrees of freedom.

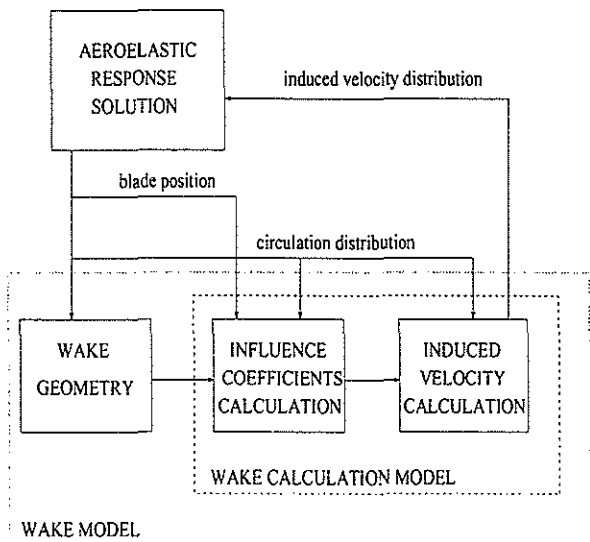


Figure 3: Wake model structure

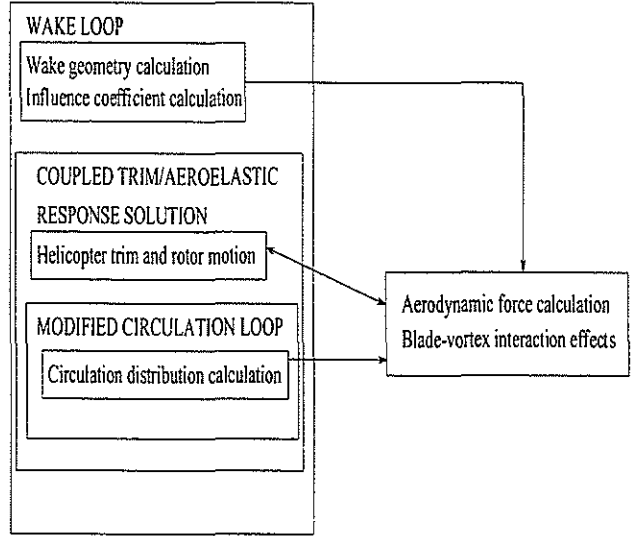


Figure 4: UCLA model: solution structure

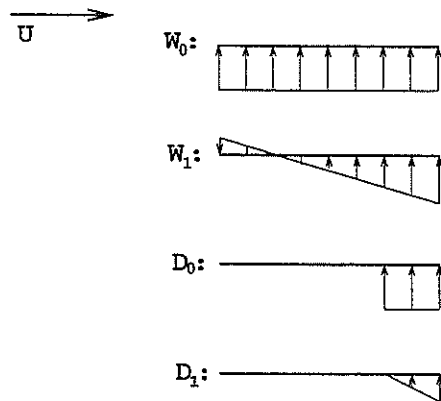


Figure 5: Normal velocity distributions corresponding to generalized airfoil and flap motions  $W_0$ ,  $W_1$ ,  $D_0$ , and  $D_1$ .

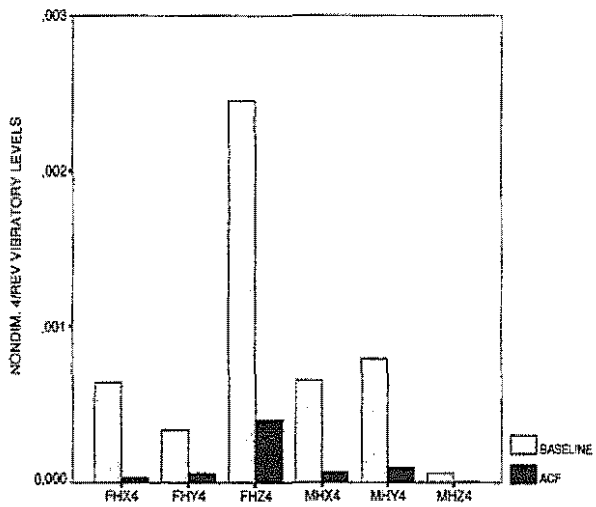


Figure 6: Simultaneous reduction of the 4/rev hub shears and moments,  $\mu = 0.15$ , RFA aerodynamics.

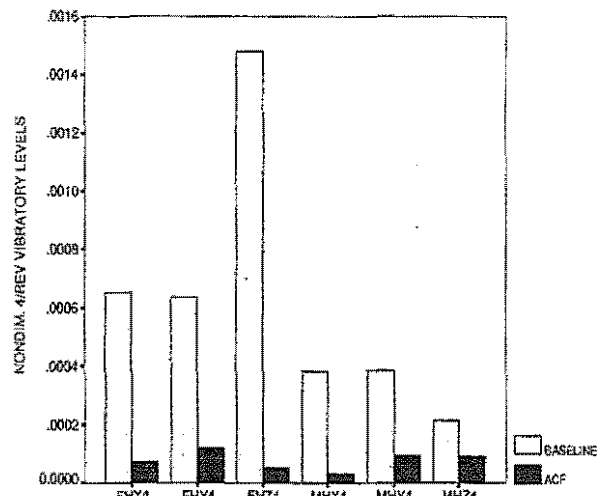


Figure 8: Simultaneous reduction of the 4/rev hub shears and moments,  $\mu = 0.30$ , RFA aerodynamics.

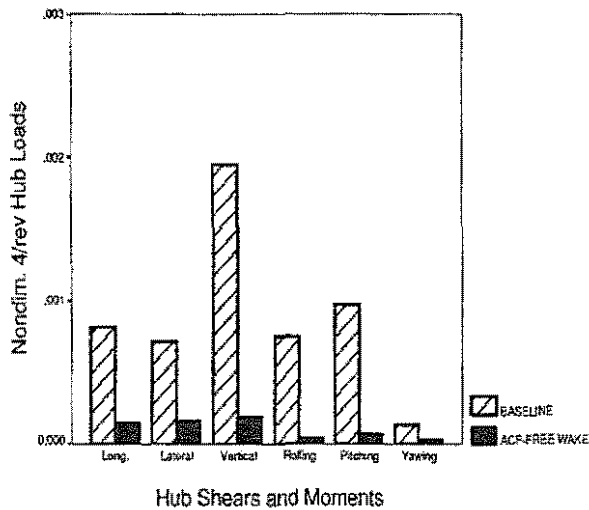


Figure 7: Simultaneous reduction of the 4/rev hub shears and moments,  $\mu = 0.15$ , quasisteady aerodynamics

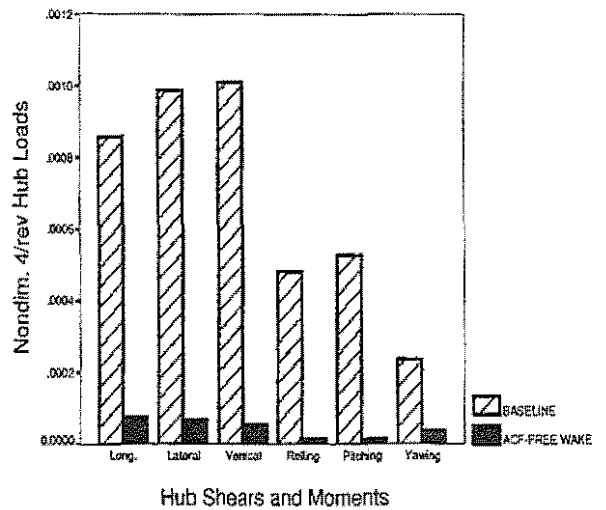


Figure 9: Simultaneous reduction of the 4/rev hub shears and moments,  $\mu = 0.30$ , quasisteady aerodynamics

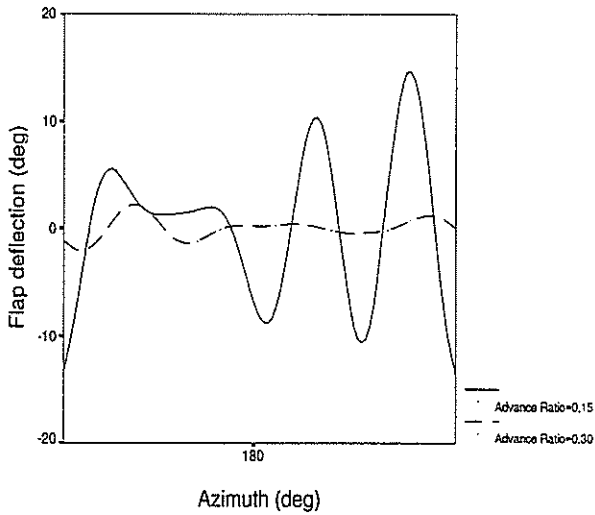


Figure 10: Flap deflection history at the advance ratios  $\mu = 0.15$  and  $\mu = 0.30$ , RFA aerodynamics.

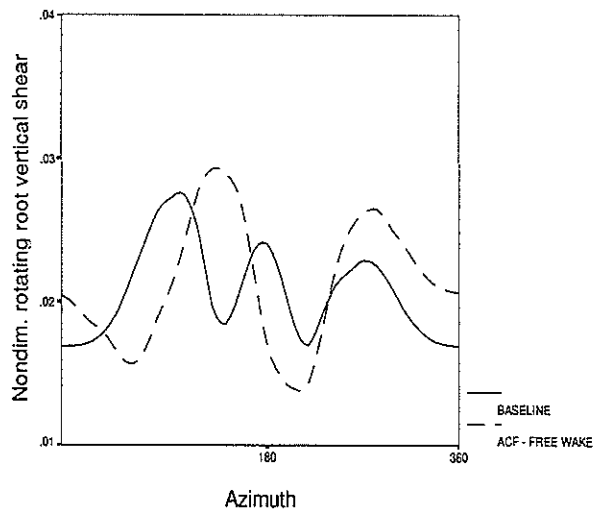


Figure 12: Nondimensional rotating root vertical shear,  $\mu = 0.15$ , quasisteady aerodynamics.

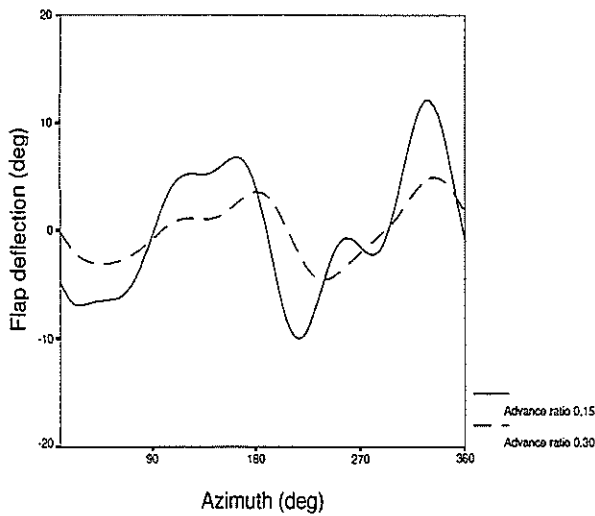


Figure 11: Flap deflection history at the advance ratios  $\mu = 0.15$  and  $\mu = 0.30$ , quasisteady aerodynamics

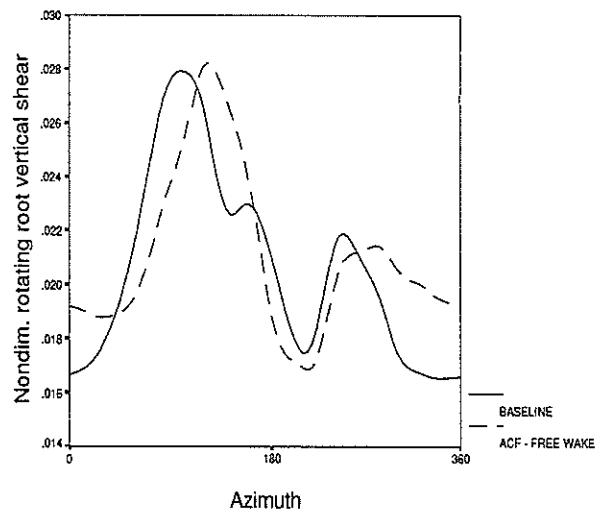


Figure 13: Nondimensional rotating root vertical shear,  $\mu = 0.30$ , quasisteady aerodynamics.

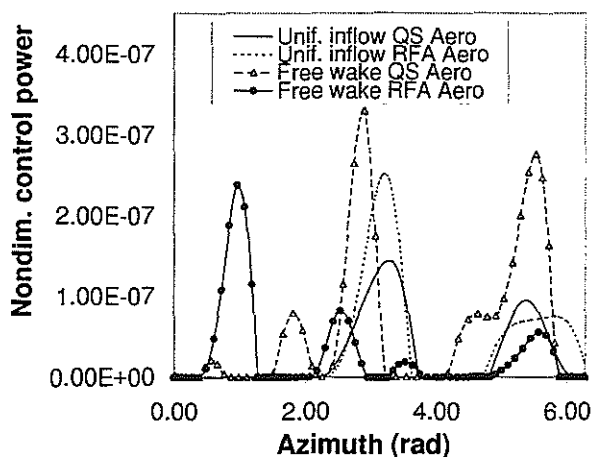


Figure 14: Control power requirements over one revolution,  $\mu = 0.30$ .

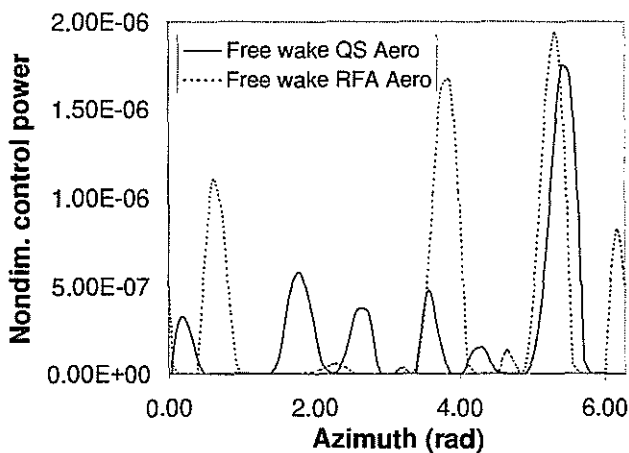


Figure 15: Control power requirements over one revolution,  $\mu = 0.15$

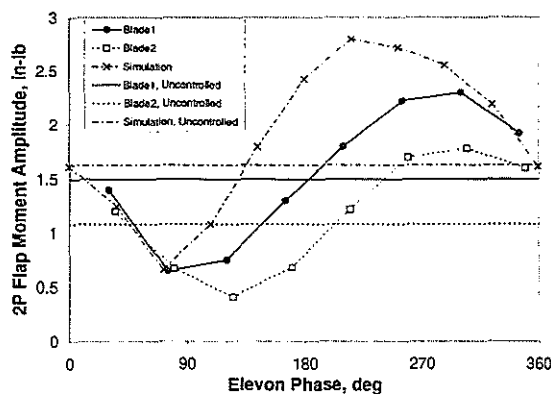


Figure 16: Variation of 2/rev flap bending moment with elevon phase (760 RPM,  $\mu = 0.20$ , quasisteady aerodynamics)

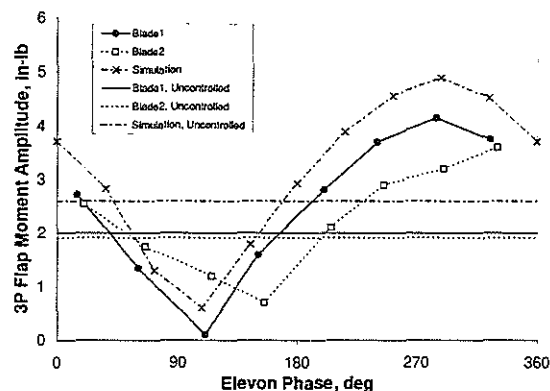


Figure 17: Variation of 3/rev flap bending moment with elevon phase (760 RPM,  $\mu = 0.20$ , quasisteady aerodynamics)

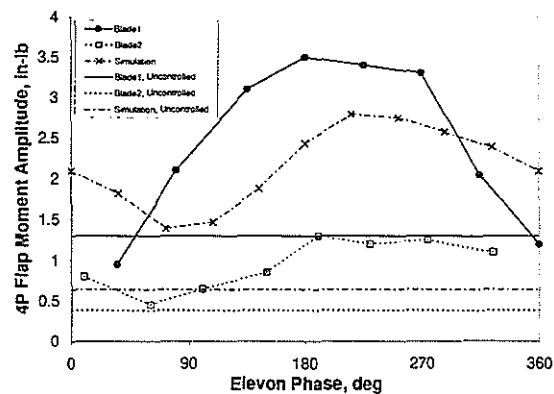


Figure 18: Variation of 4/rev flap bending moment with elevon phase (760 RPM,  $\mu = 0.20$ , quasisteady aerodynamics)

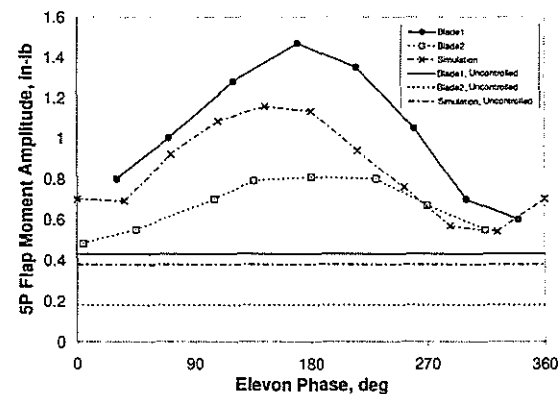


Figure 19: Variation of 5/rev flap bending moment with elevon phase (760 RPM,  $\mu = 0.20$ , quasisteady aerodynamics)

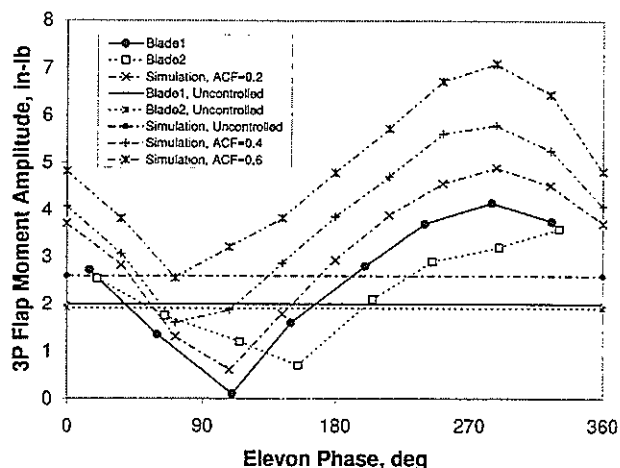


Figure 20: Effect of flap reduction coefficient  $C_f$  on 3/rev phase sweep (760 RPM,  $\mu = 0.20$ , quasisteady aerodynamics)

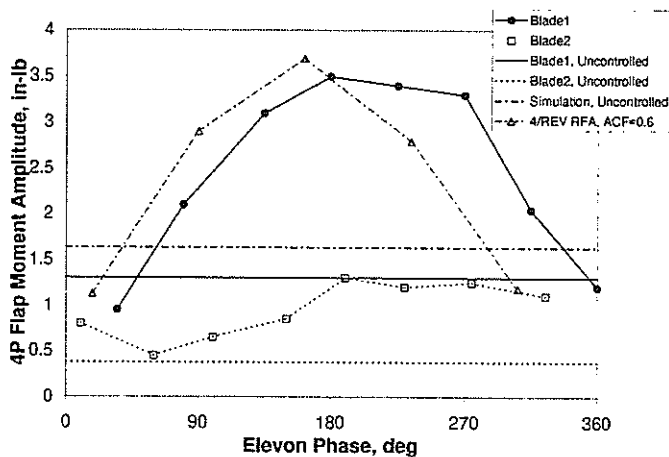


Figure 23: Variation of 4/rev flap bending moment with elevon phase (760 RPM,  $\mu = 0.20$ , RFA aerodynamics)

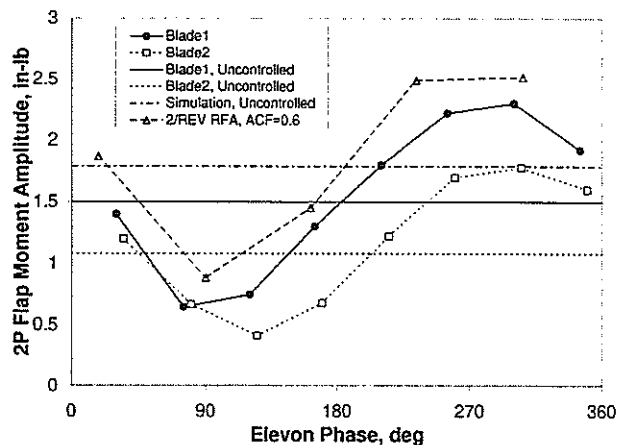


Figure 21: Variation of 2/rev flap bending moment with elevon phase (760 RPM,  $\mu = 0.20$ , RFA aerodynamics)

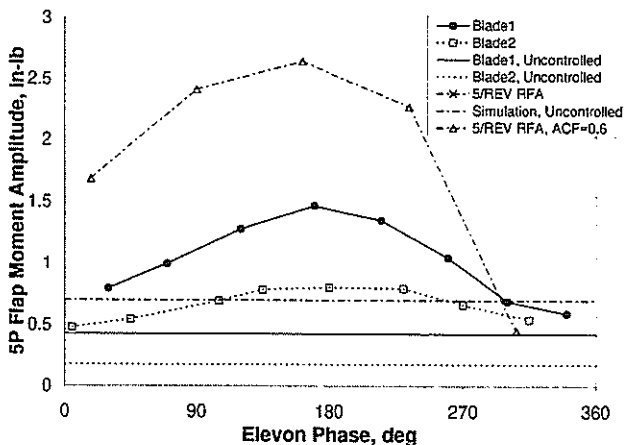


Figure 24: Variation of 5/rev flap bending moment with elevon phase (760 RPM,  $\mu = 0.20$ , RFA aerodynamics)

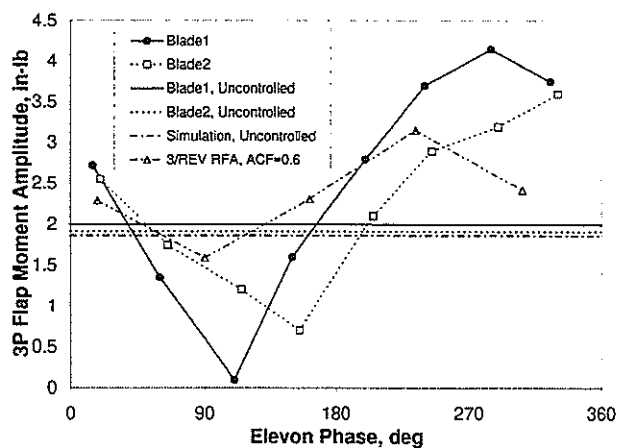


Figure 22: Variation of 3/rev flap bending moment with elevon phase (760 RPM,  $\mu = 0.20$ , RFA aerodynamics)

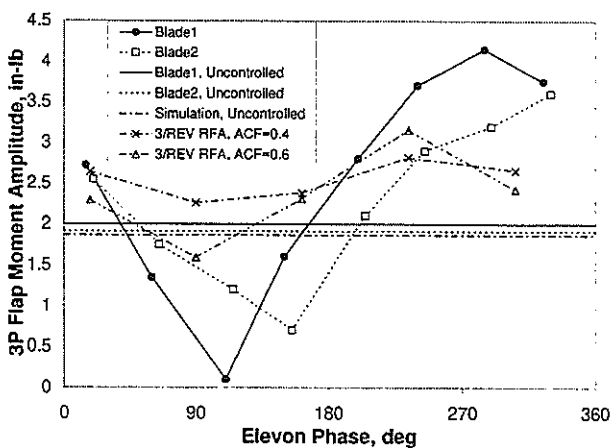


Figure 25: Effect of flap reduction coefficient  $C_f$  on 3/rev phase sweep (760 RPM,  $\mu = 0.20$ , RFA aerodynamics)